

Contents lists available at ScienceDirect

Fundamental Research

journal homepage: <http://www.keaipublishing.com/en/journals/fundamental-research/>

Article

Strong absorption in ultra-wide band by surface nano engineering of metallic glass

Jianan Fu^a, Xin Li^a, Zhen Li^a, Fei Sun^a, Wenxin Wen^a, Jinlai Zhao^b, Wenqing Ruan^a, Shuai Ren^a, Zhenxuan Zhang^a, Xiong Liang^a, Jiang Ma^{a,*}^a Shenzhen Key Laboratory of High Performance Nontraditional Manufacturing, College of Mechatronics and Control Engineering, Shenzhen University, Shenzhen 518060, China^b College of Materials Science and Engineering, Shenzhen Key Laboratory of Polymer Science and Technology, Guangdong Research Center for Interfacial Engineering of Functional Materials, Shenzhen 518060, China

ARTICLE INFO

Article history:

Received 7 April 2022

Received in revised form 10 August 2022

Accepted 13 September 2022

Available online xxx

Keywords:

Metallic glass

Nanoforming

Ultra-wideband absorption

Photothermal properties

ABSTRACT

Broadband light absorption is important for applications such as infrared detectors, solar energy collectors, and photothermal conversion. We propose a facile and common strategy to fabricate light absorbers with strong ultra-wideband absorption. Due to their excellent thermoplastic forming ability, metallic glasses could be patterned into finely arranged nanowire arrays, which show extremely low reflectivity ($\sim 0.6\%$) in the visible and near-infrared regimes, and a low reflectivity ($\sim 15\%$) in the mid-infrared regime as caused by multiscale nano spacing, multiple reflections, and plasmonic behavior. The strong absorption at surfaces with nanowires provides excellent photothermal conversion properties. The photothermal properties show that a surface with nanowires can be rapidly heated up to ~ 160 °C at a rate of 28.75 °C/s, which is 30 times higher than smooth surfaces. Meanwhile, a surface with nanowires shows a high photothermal conversion efficiency ($\eta_{PT} = 56.36\%$). The fabricated metallic glass absorbers exhibit adaptability as they can be easily formed into various complex shapes and meet the requirements under harsh conditions. The outcomes of our research open the door to manufacturing high-performance absorbers for applications in photothermal electric power generation, desalination, and photodetectors.

1. Introduction

The ideal blackbody is a perfect absorber, which can completely absorb light over a wide range and be used for photothermal (PT) conversion. To date, absorbers with near blackbody performance have been widely used as infrared detectors [1–4], solar energy collectors [5, 6], solar energy desalination [7], and other fields [8,9]. Near-blackbody absorbers are generally multilayer structures obtained by combining plasmonic metamaterials [10–12] with other materials. However, the absorption of such absorbers is limited to narrow wavelength ranges, and applicability in the field of PT conversion still needs to be boosted due to the costs and preparation cycle. Absorbers fabricated from carbon nanotubes [13] and carbon nanotube composite materials [14,15] via spraying and vapor deposition can achieve full broadband absorption and excellent PT performance, but the durability of the carbon nanotube layer on absorbers is insufficient in real environments, which hinders the further development of absorbers [16].

To date, the surfaces with nanostructures have great potential as absorbers to obtain PT converters with excellent performances [17,18].

When light hits the absorber surface, the nanostructures cause multiple reflections, which enhances light absorption [19]. Plasmonic behavior can be easily achieved by adjusting the size of nanostructures and the space between them [20,21]. Existing nanostructures also reduce the thermal conductivity of the absorber [22], which greatly benefits the PT performance. Most nanostructures have been used to enhance the absorption performances, which include cylindrical nanoholes [23], dielectric microspheres [24], nanocones [25], and nanoshells [26]. However, only narrowband absorption can be achieved through such nanostructures, and the processing methods to prepare them are complex, especially on metallic surfaces. Therefore, developing facilities to fabricate nanostructures on advanced metallic materials is crucial for strong wideband absorption with a high PT performance.

Metallic glasses (MGs) have attracted significant attention due to their excellent properties since they were discovered [27–34]. The unique atomic structure allows them to be thermoplastic formed (TPF) in certain temperature span which is called the supercooled liquid region (SLR) [35,36]. Therefore, MGs were considered as the ideal materials for the miniature fabrication [37–39]. Previous works have tried

* Corresponding author.

E-mail address: majiang@szu.edu.cn (J. Ma).<https://doi.org/10.1016/j.fmre.2022.09.017>2667-3258/© 2022 The Authors. Publishing Services by Elsevier B.V. on behalf of KeAi Communications Co. Ltd. This is an open access article under the CC BY-NC-ND license (<http://creativecommons.org/licenses/by-nc-nd/4.0/>)

to form micro/nanopatterns on MG surface and studied their PT properties [40–42]. However, this shows great limitations focused primarily on studying specific wavelengths. It is still an open question of exploring the absorption ability of MGs with nanostructures over wide wavelength ranges and the PT applications.

Here, large-area, uniform and ordered nanowire arrays were fabricated on the MG surface (Pt-MG) by utilizing TPF. The surface with Pt-MG nanowires (Pt-MG NWs) shows an extremely low broadband reflectance of less than 20% (400 nm to 20 μm), which is less than 1% from 400 to 1800 nm. We also studied the PT properties of the surface with nanostructures at five different wavelengths λ (405, 532, 655, 808, 1064 nm). When irradiating the Pt-MG NWs with an 808 nm laser at 6.4 W/cm², the surface rapidly heated up to ~ 160 °C at a rate of 28.75 °C/s. Meantime, the system exhibited a high PT efficiency ($\eta_{PT} = 56.36\%$), which is better than most reported PT materials. The prepared nanosurface with excellent broadband absorption and PT properties is expected to be applied in many PT fields, such as switching, therapy, and electric power generation. In addition, the prepared nanosurface have excellent flexibility and can be formed into complex shapes such as arc, folded, and dome, which is suitable for applications that require complex shapes.

2. Material and methods

2.1. Materials

The Pt-based MG system (Pt-Ni-Cu-P) was selected as it has excellent flow properties and thermal stability in the SLR [35,37]. An MG rod with a diameter of ~ 5 mm was prepared from an alloy ingot with a nominal composition of Pt_{57.5}Cu_{14.7}Ni_{5.3}P_{22.5} by conventional water-cooled copper mold casting. The prepared Pt-MG rod was cut into disks with thicknesses of ~ 1 mm, and both sides of the disks were polished to reduce the influence of surface roughness.

2.2. TPF

The polished MG disks were stacked with the anodic aluminium oxide (AAO) template using a through hole having a diameter of ~ 200 nm, which was then placed in a heated vacuum chamber. After the vacuum was below 10^{-3} Pa, the sample was heated to its SLR (see Fig. S2) at a heating rate of 60 K/min. A pressure of 300 MPa was applied to the specimens at a rate of 0.05 mm/s and was maintained for 10 s. The pressure was then quickly removed, and the specimen was removed from the chamber.

2.3. Secondary tpf (STPF)

The AAO template was retained to avoid nanowire destruction in the STPF. The samples with an undissolved AAO template were heated to ~ 515 K, and the samples were treated via STPF. After the temperature was cooled to room temperature, 15 wt% NaOH solution was used to dissolve the AAO template remaining on the sample surface.

2.4. Reflectance simulation

The Pt-MG NWs with a diameter of 200 nm and a length of 1600 nm were formed on the MG surface via TPF. The 3D model of the Pt-MG NWs was established based on this parameter (see Fig. S3), and periodic boundary conditions were set to simulate the periodic nanowire arrays. The physical wave optical field was selected after setting the material of the Pt-MG NWs. A visible light source (wavelength range from 400 to 750 nm with a step size of 5 nm) was vertically incident on the established model, and the reflectance under the model was obtained.

2.5. PT effect

The laser with wavelengths of 405 nm (PGL-V-H-405), 532 nm (PGL-V-H-532), 655 nm (PGL-V-H-655), 808 nm (5 W, fiber-tailed, multimode diode laser), and 1064 nm (PGL-V-H-1064) were used to characterize the PT effect of the samples. The sample was placed on quartz, the laser switch cycle was 100 s, and the laser irradiated the sample vertically till 450 s. An infrared imaging camera was used to monitor the thermal response of the MG surface during this process.

2.6. Multiscale structural characterization

X-ray diffraction (XRD; RIGAKU miniflex600) with Cu K α radiation and differential scanning calorimetry (DSC; Perkin-Elmer DSC-8000) at a heating rate of 20 K/min were used to detect the amorphous nature of the Pt-MG plate and Pt-MG NWs. Scanning electron microscope (SEM; Fei quanta FEG 450) was applied to determine the morphology of Pt-MG NWs on the MG surface. The reflectance of the sample in the visible regime (400–800 nm) was measured using a microspectral measurement system (Hangzhou SPL; ProSp-Micro40-VIS). Fourier transform infrared spectrometer (Vertex 70; Bruker) with an integrating sphere was used to measure the sample reflectance in the NIR and MIR regimes. A gold mirror was used as the reference sample. An infrared imaging camera (Fotric 286) with a data acquisition frequency of 1 Hz collected thermal images. The optical constants of Pt-MG were measured with an ellipsometer (VE-mapping) at incidence angles of 70° over wavelengths of 400–750 nm. The atomic structure was characterized in a JEM-2100F TEM with energy disperse spectroscopy (EDS).

3. Results and discussion

3.1. Nano engineering of Mg surface

A schematic diagram for the fabrication of uniform and ordered nanowire arrays over a large area is shown in Fig. 1a. The nanowires can be rapidly fabricated on the MG surface via TPF. The morphology of the prepared nanowires is shown in Fig. 1b (see Fig. S1). The large area of the Pt-MG NWs grows densely on the MG surface and shows a uniform distribution. These Pt-MG NWs are self-supporting structures that endow themselves with excellent durability [43]. The details of the nanowire arrays are depicted in Fig 1c. The spacing between nanowires is also at the nanoscale, which helps capture light [44]. The average diameter of Pt-MG NWs is counted based on the SEM image, and the results are summarized in Fig. 1d. The average diameter of the Pt-MG NWs is consistent with the nanoscale cavity size (~ 200 nm) of the AAO template. Both the as-cast Pt-MG plate and surface with Pt-MG NWs show fully amorphous structures, which can be ascertained from the XRD patterns in Fig. 1e. This means that the Pt-MG NWs on the MG surface are destroyed, and the glassy surface can be reused to help restructure the nanowires via TPF (see Fig. S4). Fig. 1f shows the morphology of a single nanowire under low-resolution TEM, and the corresponding high-resolution TEM image is displayed in Fig. 1g. The disordered atomic structure in nanowires indicates that they are in a glassy state. The selected area electron diffraction image of the halo ring shown in the inset agrees with the high-resolution TEM image. The elemental distribution of the nanowire is displayed in Fig. 1h, where the elements of Pt, Cu, Ni and P are uniformly distributed. These results demonstrate that we can fabricate precise and dense nanostructures on MGs through a facile method due to their excellent TPF abilities.

3.2. Reflectance of Pt-MG NWs

The MGs exhibit significant optical change due to the nanostructures. As shown in Fig. 2a, the surface with the Pt-MG NWs becomes dark black

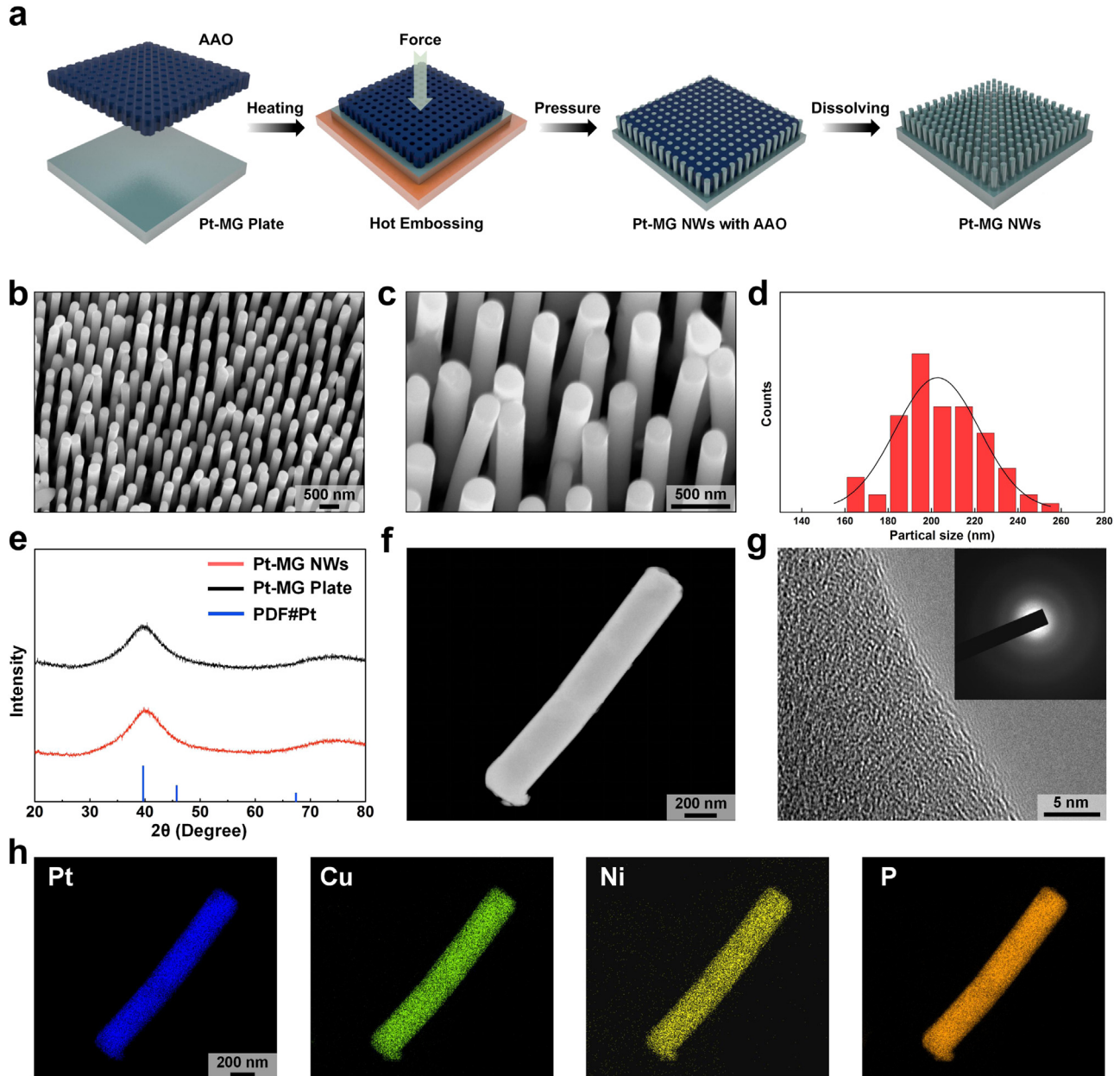


Fig. 1. Fabrication and characterization of Pt-MG NWs. (a) Schematic diagram of the Pt-MG NWs fabrication. (b) Micromorphology of the Pt-MG NWs under low magnification. (c) Micromorphology of the Pt-MG NWs under high magnification. (d) Size distribution of the Pt-MG NWs. (e) XRD patterns of the Pt-MG NWs and Pt-MG plate. (f) Morphology of a single Pt-MG NW. (g) High-resolution TEM image of the Pt-MG NW, where the inset is a selected area electron diffraction image. (h) Element distribution of the Pt-MG NW.

when exposed to natural environments, which means it is an excellent light absorber. The optical constants of the Pt-MG are measured to quantitatively investigate the optical properties of the nanosurface. Fig. 2b and c show the refractive index (n) and extinction coefficient (k) of the Pt-MG. The absorption properties of surfaces with Pt-MG NWs are simulated via wave optics (COMSOL) that combine the optical constants and size parameters of Pt-MG NWs. The COMSOL simulated spectra are presented in Fig. 2d. The simulated surface exhibits a low reflectance (< 5%) from 400 to 750 nm. Thus, the absorption of the simulated surface reaches more than 95% by the following Eq. (1):

$$A = 1 - R - T \quad (1)$$

where A represents the absorption, R is the reflectance, and T is the transmittance. The T is chosen to be zero (see Fig. S5) [10].

To understand the reflection mechanism of the nanosurface, we propose the possible interactions between light and Pt-MG NWs, as shown in Fig. 2e. When light hits the nanosurface, the spacing between nanowires captures the light, which is reflected multiple times between nanowires. Each reflection increases the light path and causes part of it to be absorbed. Multiple reflections also greatly increase the absorption of the nanosurface, which is verified by the electric field distribution in the nanowires as observed at three specific wavelengths (see Fig. 2f). The electric field distributions on the Pt-MG NWs shows the formation of standing waves on their surface. The formation of hot spots on the Pt-MG NWs is due to the coherent phase length of the light, which indicates the light is strongly localized around the nanowires. Therefore, the electric field distribution spots on all the nanowires indicate the strength of the light binding ability.

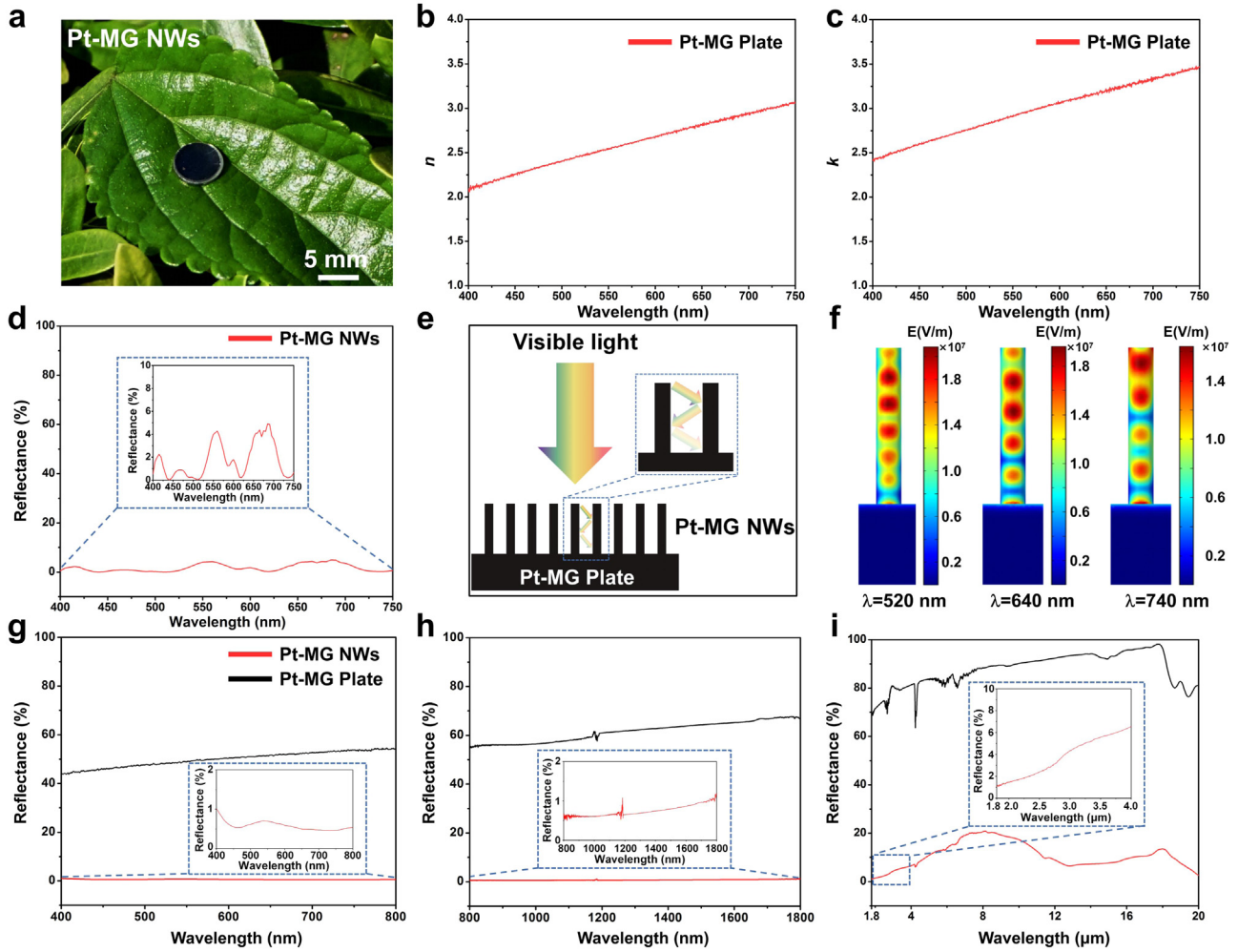


Fig. 2. Optical properties of Pt-MG NWs. (a) Photograph of the MG surface with the Pt-MG NWs. (b) Refractive index of Pt-MG. (c) Extinction coefficient of Pt-MG. (d) Simulated spectra of Pt-MG NWs from 400 to 750 nm. (e) Schematic diagram of the interactions between visible light and nanowires. (f) Electric field distributions at wavelengths of 520, 640, and 740 nm. (g) Reflection spectrum of the Pt-MG plate and Pt-MG NWs from 400 to 800 nm. (h) Reflection spectrum of the Pt-MG plate and Pt-MG NWs from 800 to 1800 nm. (i) Reflection spectrum of the Pt-MG plate and Pt-MG NWs from 1.8 to 20 μm .

It is noted that the electric field distribution in the spots weakens from the top to the bottom, and the surface light is gradually absorbed between the nanowires. Meanwhile, as the nanowires are arranged in the simulations, a high density of surface plasmon polariton (SPP) mode is excited at the hot spots, which results in their broadband absorption. Based on the simulation results, we measured the reflectance spectrum of the surface with Pt-MG NWs. The experimental reflectance spectrum (400 nm to 20 μm) is shown in Fig. 2g-i, and the reflection spectrum of Pt-MG plate is also summarized as a comparison. The surface with Pt-MG NWs exhibits extremely low reflectivity ($\sim 0.6\%$) in the visible and near-infrared (NIR) regimes and a low reflectivity ($\sim 15\%$) in the mid-infrared (MIR) regime. These results, which are superior to the simulation results, are attributed to the slight tilt of some Pt-MG NWs growing on the surface. The partial tilt of Pt-MG NWs leads to the multiscale spacing between nanowires, which captures different light wavelengths.

Furthermore, the experimental Pt-MG NW arrays are a mixed arrangement of ordered and disordered compared with the simulated ordered arrangement of Pt-MG NWs. There was some aggregation of Pt-MG NWs in the prepared structures, and optical simulations were performed. A significantly enhanced electric field was observed on the interdependent Pt-MG NWs (see Fig. S6), which indicates excitations of high-density localized surface plasmon resonance (LSPR) in the experimental Pt-MG NWs. The results indicate that the experimental results

are better than the simulations, which leads to its excellent broadband (400 nm to 20 μm) absorption performance [45,46].

3.3. PT conversion property of nano engineering surface

The surface with Pt-MG NWs shows a very low reflectance and high absorption for wavelengths from 400 nm to 20 μm , which is expected to play a crucial role in the energy field. Thus, the PT conversion performance of the surface with Pt-MG NWs is investigated, as illustrated in Fig. 3a. The tested samples were placed horizontally on quartz plates. The switching frequency of the laser is periodically controlled to irradiate the sample surface, and an infrared camera is used to record temperature changes at the surface. Fig. 3b shows the PT response of the surface with Pt-MG NWs irradiated by NIR light at 808 nm (power density from 0.8 to 6.4 W/cm^2). It is noted that the temperature of the surface with Pt-MG NWs increases to 160 (see Video S1), 134, 82, 54.9, and 41.6 $^{\circ}\text{C}$ rapidly at power densities of 6.4, 4.8, 3.2, 1.6, and 0.8 W/cm^2 , respectively. Thus, the surface with Pt-MG NWs shows an excellent and controllable PT performance when irradiated by NIR light.

After the Pt-MG NWs have been placed for some time, a repeatability experiment was performed on the Pt-MG NWs using the 808 nm laser at different power densities (see Fig. S7). The Pt-MG NWs also show rapid heating, and the maximum temperature (T_{max}) of the surface remains

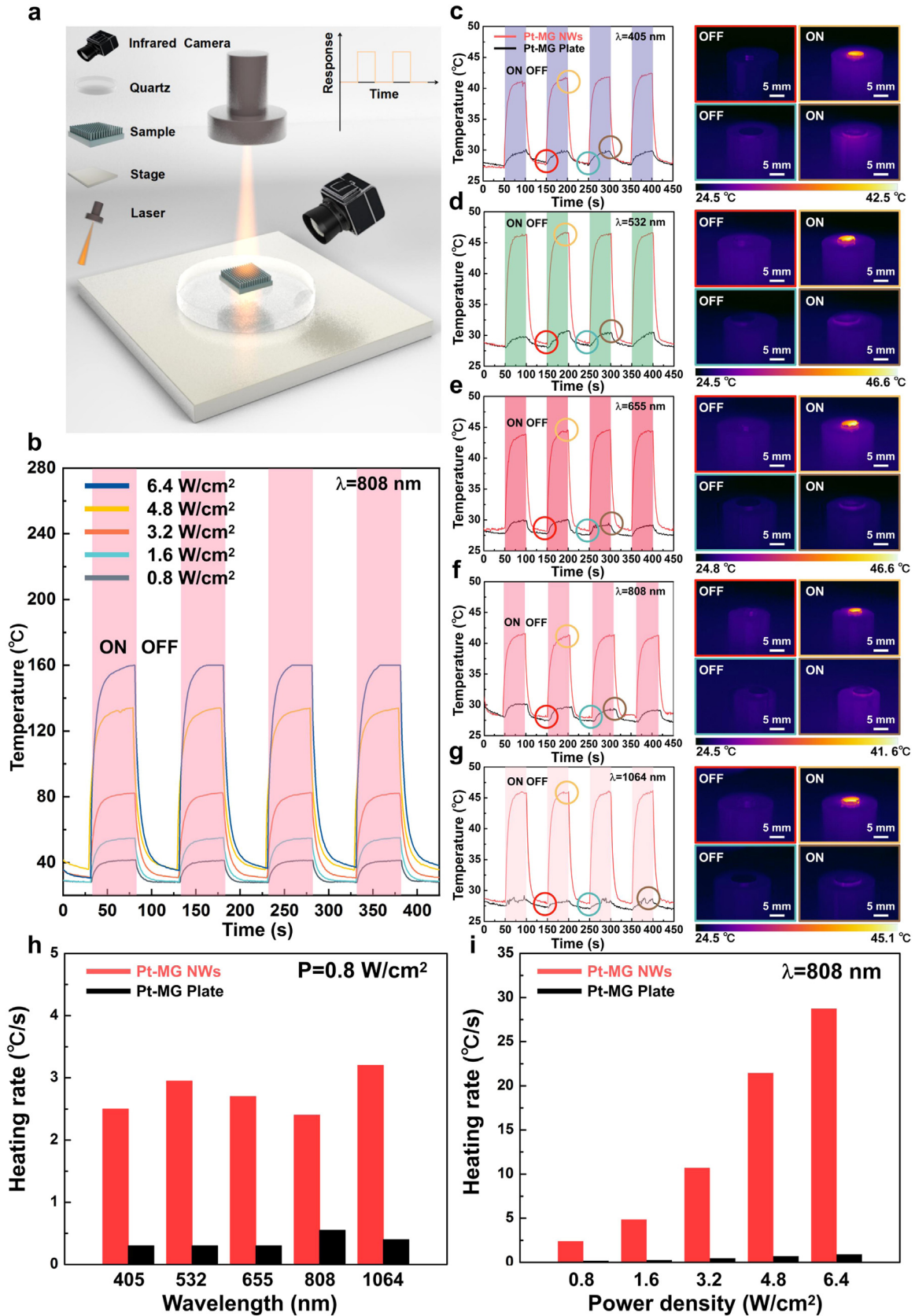


Fig. 3. The PT conversion performance of Pt-MG NWs. (a) Schematic diagram to test the PT performance of Pt-MG NWs. (b) PT cyclic curve of Pt-MG NWs irradiated by an 808 nm laser at different power densities. (c) PT cyclic curve of Pt-MG NWs and Pt-MG plate irradiated by 405 nm laser at 0.8 W/cm², (d) at 532 nm, (e) at 655 nm, (f) at 808 nm, and (g) at 1064 nm. (h) Heating rate of the Pt-MG plate and Pt-MG NWs under different wavelengths at 0.8 W/cm². (i) Heating rate of the Pt-MG plate and Pt-MG NWs under different power densities at 808 nm.

Table 1
Summary of the various PT materials for η_{PT} , T_{max} , and heating rate.

Sample	η_{PT}	T_{max} (°C)	Heating Rate (°C/s)	Ref.
Pt-MG NWs	56.36%	160	28.75	This work
ZnPB-3	39.79%	63.4	0.123	[51]
Zr-PDI	52.3%	160	16	[50]
Cu ₁₀ MOF	/	48.4	0.078	[52]
CuS@HKUST-PDA	/	57	0.1067	[53]
Cocrystals	18.8%	71.3	0.1188	[54]
CuS/GO	/	54	0.048	[55]
Mg/H-PCL/ICG	/	52.3	0.0275	[56]
NH2-MIL-125-GO-Pt	/	54.2	0.081	[57]
Cu _{2-x} Se Nanocrystal	22%	58	0.0183	[58]
sSMONRs-PDMS	/	400	20	[59]
CS-3	22.26%	56	0.47	[60]
Au-CuS_T_FW	30.56%	31	0.015	[61]
P1 NPs	30.1%	64.8	0.216	[62]
Au-Cu ₉ S ₅ NPs	37%	50	0.417	[63]
Fe ₃ O ₄ @CuS-PEG NP	19.2%	60	0.0583	[64]

nearly the same as in previous experiments under different irradiation power densities. The results indicate that the PT performance of the surface with Pt-MG NWs has good repeatability. In addition, the PT responses of the Pt-MG plate and surface with Pt-MG NWs irradiated by wavelengths of 405, 532, 655, 808, and 1064 nm at a constant power density of 0.8 W/cm² are shown in Fig. 3c–g. The IR images of the samples with the highest and lowest temperatures under these illuminations are on the right side. When different wavelengths irradiate the surface, the temperature rise for the Pt-MG plate is only ~2 °C, but when the Pt-MG NWs are introduced, the temperature rapidly reaches ~44 °C. This demonstrates that surfaces with Pt-MG NWs can absorb light of different wavelengths and rapidly convert it into thermal energy.

Surfaces with Pt-MG NWs still show excellent PT performance after three alternating irradiation cycles, as shown in Fig. 3c–g. Thus, the Pt-MG NWs have a high PT stability under laser irradiation of different wavelengths. Fig. 3h summarizes the heating rate of the Pt-MG NWs and Pt-MG plate under laser irradiation of different wavelengths at power densities of 0.8 W/cm². The surface with Pt-MG NWs shows a much higher heating rate than Pt-MG plate, indicating the enhanced surface heating rate is fully ascribed to the Pt-MG NWs. The heating rates of the Pt-MG NWs and Pt-MG plate at different power densities are illustrated in the Fig. 3i. The heating rate at the surface with Pt-MG NWs increases sharply with the power density. When the power density increases to 6.4 W/cm², the surface shows a heating rate of 28.75 °C/s. The Pt-MG plate also increases with the power density, but at a relatively slow rate of about 0.9 °C/s, which is far lower than the surface with Pt-MG NWs. Based on the cooling rate curve for Pt-MG NWs (see Fig. S8), the η_{PT} of Pt-MG NWs is calculated as 56.36% by the energy balance equation [47–50]:

$$\sum_i m_i C_{i,p} \frac{dT}{dt} = Q - Q_{loss} \quad (2)$$

where m_i and $C_{i,p}$ are the mass and heat capacity of the system, Q is the heat energy to the Pt-MG NWs, and Q_{loss} is the thermal energy lost to the environment. (The calculation details are shown in the Supplementary Note).

We subsequently summarized the PT performance of some materials (see Table 1). Compared to the previously reported η_{PT} and heating rate exhibited by various PT materials, such as Zr-PDI (η_{PT} is 52.3%, heating rate is 16 °C/s) and ZnPB-3 (η_{PT} is 39.79%, heating rate is 0.123 °C/s), the Pt-MG NWs exhibit the best performance in both the η_{PT} and heating rate. In addition, the Pt-MG NWs also exhibit a higher T_{max} under laser irradiation than most reported PT materials such as CuS@HKUST-PDA (T_{max} is 57 °C) and Cocrystals (T_{max} is 71.3 °C). These results indicate that surfaces with Pt-MG NWs have an excellent PT conversion performance, PT stability and a high heating rate. These properties provide

promising PT applications, such as seawater desalination, and PT therapy.

In this regard, we performed desalination using the Pt-MG NWs. When 1 μ L of 3.5% wt NaCl solution was dropped on the Pt-MG NWs and Pt-MG plate, the NaCl solution was still present on the Pt-MG plate after 300 s of irradiation with the 808 nm laser. However, water in the NaCl solution on the Pt-MG NWs completely evaporated, and the formation of NaCl particles was observed from the Pt-MG NWs (see Fig. S9a). This indicates that the PT performance of Pt-MG NWs promotes water evaporation. The evaporation performance of water for the Pt-MG NWs and Pt-MG plate was also evaluated under 1 kW/m² solar irradiation. The evaporation rate of Pt-MG NWs is twice as high as the evaporation rate of Pt-MG plate (see Fig. S9b), which implies that Pt-MG NWs have practical applications in desalination.

3.4. Flexible nano engineering of MG surface

The samples remain amorphous after forming Pt-MG NWs on its surface by TPF, which provides the surface with Pt-MG NWs to carry out STPF. Fig. 4a shows the STPF process. Then, the arc, folded, and dome surfaces are formed with Pt-MG NWs (see Fig. 4b–d), and the surfaces remain black after STPF. The left, middle, and right positions of the arc surface are observed by SEM, and the Pt-MG NWs on the surface did not change (see Fig. 4e), indicating the STPF has no effect on the Pt-MG NWs and the surface still has a very strong optical absorption (see Fig. S10). We also investigate the intrinsic characteristics of the Pt-MG NWs after STPF, and the samples are fully amorphous (see Fig. S11). The high-resolution TEM image of the nanowire after STPF is shown in Fig. 4f. The disordered atomic structure under high-resolution TEM (see Fig. 4g) indicates the nanowire is also amorphous. Thus, the glassy properties have not changed after STPF, and complex structures could be formed. The elemental distribution of the nanowire is shown in Fig. 4h, which is consistent with the materials used. We believe that the surface with the Pt-MG NWs can be customized with various shapes, which broadens its applications in some fields, such as foldable PT electric power generation devices and wearable light-thermal management devices.

The nanosurface has a strong absorption over a wide range compared with the reported literature. Fig. 5 summarizes an absorption of more than 80%, as reported previously. This includes carbon nanotubes, nanocomposites, nanostructured materials, and metamaterials. These previously reported absorbers can achieve high absorption but over narrow ranges. For example, the taper arrays of the alumina–chrome multilayered metamaterial (Al-Cr metamaterial/Au) exhibit an absorption range from 400 nm to 3200 μ m, and that for a Ta absorber of multi-walled carbon nanotubes (Ta/MWCNTs) is from 300 nm to 1100 nm. The absorption range (400 nm to 20 μ m) of the Pt-MG NWs is superior to most previously reported materials. In addition, the surface with the Pt-MG NWs contributes to the engineering applications due to the advantages of easy processing and flexibility.

4. Conclusion

In summary, we developed a facile method to generate a surface absorber with excellent absorption using the TPF process. The large area Pt-MG NWs are grown on the surface and exhibit a very low broadband reflectance (400 nm to 20 μ m). The results are ascribed to the multiscale nano spacing, multiple reflection and plasmonic behavior. We also explore the PT effect of the surface and the characteristics of surface flexibility, which provides a promising route for the applications of the surface.

Declaration of competing interest

The authors declare that they have no conflicts of interest in this work.

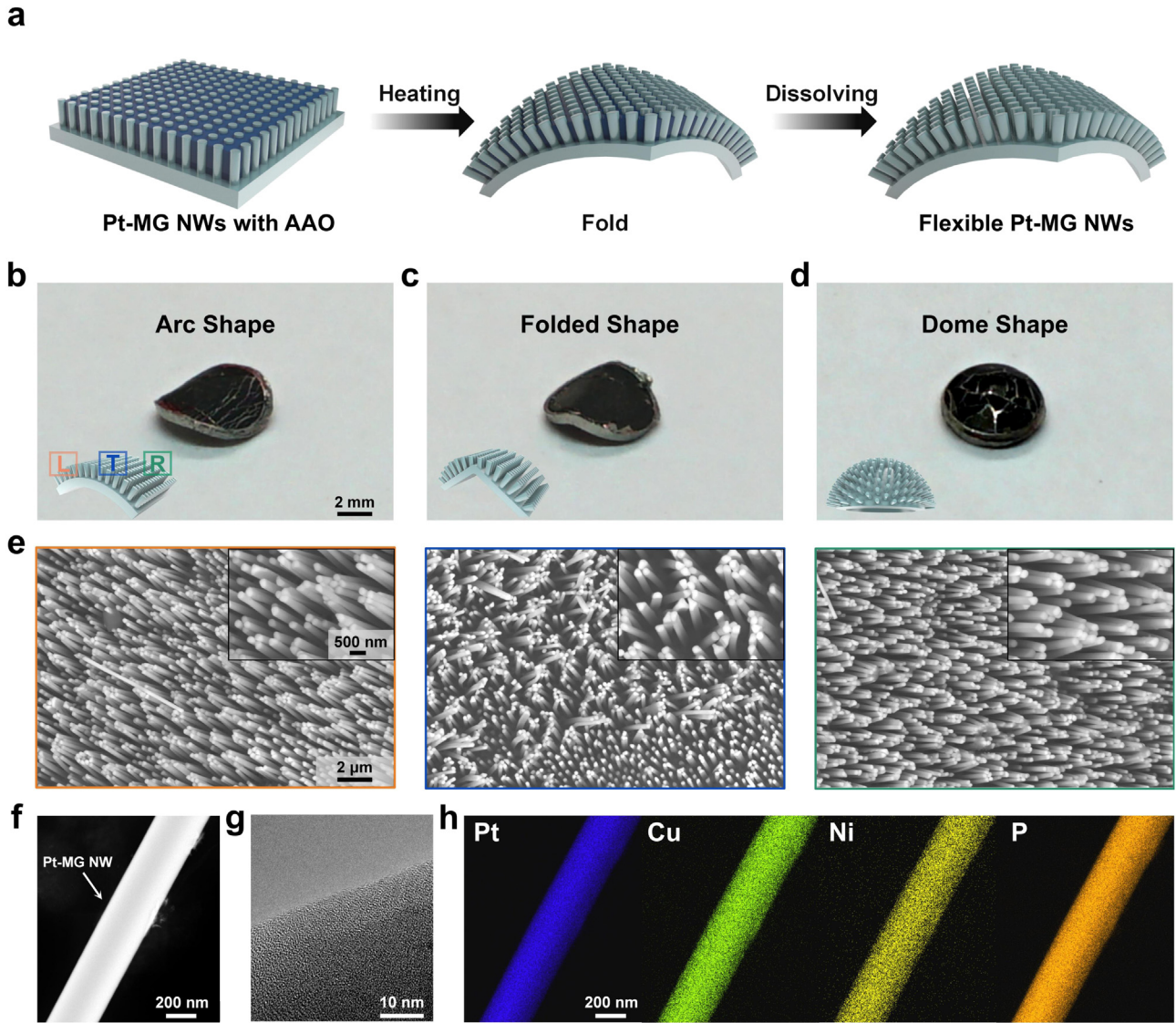


Fig. 4. The flexible MG surface with Pt-MG NWs. (a) Schematic diagram of nanosurface via STPF. (b) Nanosurface of arc shape. (c) The folded shape. (d) The dome shape. (e) SEM images of the arc nanosurface on the left, top, and right. (f) Morphology of a single Pt-MG NW after STPF. (g) High-resolution TEM image of a Pt-MG NW after STPF. (h) Element distribution of a Pt-MG NW after STPF.

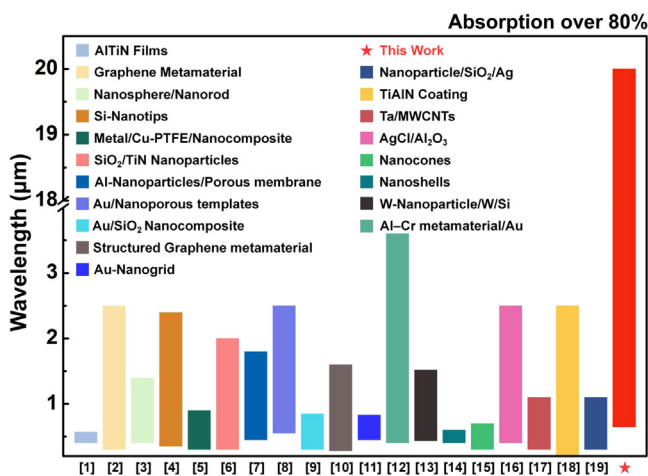


Fig. 5. Comparison of the absorption ranges between this work and previous reports. (more details in Table S1).

Acknowledgements

The work was supported by the Key Basic and Applied Research Program of Guangdong Province, China (Grant No. 2019B030302010), the National Natural Science Foundation of China (Grants Nos. 51871157, and 51971150), the National Key Research and Development Program of China (Grant No. 2018YFA0703604). The authors also thank the assistance on microscope observation received from the Electron Microscope Center of the Shenzhen University.

Supplementary materials

Supplementary material associated with this article can be found, in the online version, at [doi:10.1016/j.fmre.2022.09.017](https://doi.org/10.1016/j.fmre.2022.09.017).

References

- [1] J. You, Y. Yu, K. Cai, et al., Enhancement of MoTe₂ near-infrared absorption with gold hollow nanorods for photodetection, *Nano Res/* 13 (6) (2020) 1636–1643.
- [2] Y. Ji, W. Xu, D. Li, et al., Semiconductor plasmon enhanced monolayer upconversion nanoparticles for high performance narrowband near-infrared photodetection, *Nano Energy* 61 (2019) 211–220.

- [3] W. Li, J. Valentine, Metamaterial perfect absorber based hot electron photodetection, *Nano Lett.* 14 (6) (2014) 3510–3514.
- [4] N. Zhou, L. Gan, R. Yang, et al., Nonlayered two-dimensional defective semiconductor γ -Ga₂S₃ toward broadband photodetection, *ACS Nano* 13 (6) (2019) 6297–6307.
- [5] W. Wang, H. Wen, J. Shi, et al., An ultrathin, nanogradient, and substrate-independent WO_x-based film as a high performance flexible solar absorber, *Sol. RRL* 3 (10) (2019) 1900180.
- [6] K. Hans, S. Latha, P. Bera, et al., Hafnium carbide based solar absorber coatings with high spectral selectivity, *Sol. Energy Mater. Sol. Cells* 185 (2018) 1–7.
- [7] X. Li, W. Xu, M. Tang, et al., Graphene oxide-based efficient and scalable solar desalination under one sun with a confined 2D water path, *Proc. Natl. Acad. Sci. USA* 113 (49) (2016) 13953–13958.
- [8] M. Gao, L. Zhu, C.K. Peh, et al., Solar absorber material and system designs for photothermal water vaporization towards clean water and energy production, *Energy Environ. Sci.* 12 (3) (2019) 841–864.
- [9] X. Dai, X. Zhao, Y. Liu, et al., Controlled synthesis and surface engineering of Janus Chitosan-gold nanoparticles for photoacoustic imaging-guided synergistic gene/photothermal therapy, *Small* 17 (11) (2021) 2006004.
- [10] K. Aydin, V.E. Ferry, R.M. Briggs, et al., Broadband polarization-independent resonant light absorption using ultrathin plasmonic super absorbers, *Nat. Commun.* 2 (1) (2011) 1–7.
- [11] F. Ding, Y. Jin, B. Li, et al., Ultrabroadband strong light absorption based on thin multilayered metamaterials, *Laser Photon. Rev.* 8 (6) (2014) 946–953.
- [12] W. Li, Z.J. Coppens, L.V. Besteiro, et al., Circularly polarized light detection with hot electrons in chiral plasmonic metamaterials, *Nat. Commun.* 6 (1) (2015) 1–7.
- [13] K. Cui, B.L. Wardle, Breakdown of native oxide enables multifunctional, free-form carbon nanotube–metal hierarchical architectures, *ACS Appl. Mater. Interfaces* 11 (38) (2019) 35212–35220.
- [14] Y. Jin, T. Zhang, J. Zhao, et al., Spray coating of a perfect absorber based on carbon nanotube multiscale composites, *Carbon N Y* 178 (2021) 616–624.
- [15] M. Zhang, D. Ban, C. Xu, et al., Large-area and broadband thermoelectric infrared detection in a carbon nanotube black-body absorber, *ACS Nano* 13 (11) (2019) 13285–13292.
- [16] T. Xu, H. Shi, Y.K. Wu, et al., Structural colors: from plasmonic to carbon nanostructures, *Small* 7 (22) (2011) 3128–3136.
- [17] J. Gao, X. Wu, Q. Li, et al., Template-free growth of well-ordered silver nano forest/ceramic metamaterial films with tunable optical responses, *Adv. Mater.* 29 (16) (2017) 1605324.
- [18] S.C. Singh, M. Elkabbash, Z. Li, et al., Solar-trackable super-wicking black metal panel for photothermal water sanitation, *Nat. Sustain.* 3 (11) (2020) 938–946.
- [19] A.G. Wattoo, R. Bagheri, X. Ding, et al., Template free growth of robustly stable nanophotonic structures: broadband light superabsorbers, *J. Mater. Chem. C* 6 (32) (2018) 8646–8662.
- [20] R. Atkinson, W.R. Hendren, G.A. Wurtz, et al., Anisotropic optical properties of arrays of gold nanorods embedded in alumina, *Phys. Rev. B* 73 (23) (2006) 235402.
- [21] W. Dickson, G. Wurtz, P. Evans, et al., Dielectric-loaded plasmonic nanoantenna arrays: a metamaterial with tuneable optical properties, *Phys. Rev. B* 76 (11) (2007) 115411.
- [22] M. Goyal, Shape, size and phonon scattering effect on the thermal conductivity of nanostructures, *Pramana* 91 (6) (2018) 1–5.
- [23] P. Molet, J.L. Garcia-Pomar, C. Matricardi, et al., Ultrathin semiconductor superabsorbers from the visible to the near-infrared, *Adv. Mater.* 30 (9) (2018) 1705876.
- [24] Z. Liu, L. Liu, H. Lu, et al., Ultra-broadband tunable resonant light trapping in a two-dimensional randomly microstructured plasmonic-photonics absorber, *Sci. Rep.* 7 (1) (2017) 1–9.
- [25] K.X. Wang, Z. Yu, V. Liu, et al., Absorption enhancement in ultrathin crystalline silicon solar cells with antireflection and light-trapping nanocone gratings, *Nano Lett.* 12 (3) (2012) 1616–1619.
- [26] Y. Yao, J. Yao, V.K. Narasimhan, et al., Broadband light management using low-Q whispering gallery modes in spherical nanoshells, *Nat. Commun.* 3 (1) (2012) 1–7.
- [27] W. Klement, R. Willens, P. Duwez, Non-crystalline structure in solidified gold–silicon alloys, *Nature* 187 (4740) (1960) 869–870.
- [28] A. Inoue, Stabilization of metallic supercooled liquid and bulk amorphous alloys, *Acta Mater.* 48 (1) (2000) 279–306.
- [29] C.A. Schuh, T.C. Hufnagel, U. Ramamurty, Mechanical behavior of amorphous alloys, *Acta Mater.* 55 (12) (2007) 4067–4109.
- [30] W.L. Johnson, Bulk glass-forming metallic alloys: science and technology, *MRS Bull.* 24 (24) (1999) 42–56.
- [31] W.-H. Wang, C. Dong, C. Shek, Bulk metallic glasses, *Mater. Sci. Eng. R* 44 (2–3) (2004) 45–89.
- [32] J. Ma, C. Yang, X. Liu, et al., Fast surface dynamics enabled cold joining of metallic glasses, *Sci. Adv.* 5 (11) (2019) eaax7256.
- [33] X. Li, D. Wei, J. Zhang, et al., Ultrasonic plasticity of metallic glass near room temperature, *Appl. Mater. Today* 21 (2020) 100866.
- [34] J. Fu, J. Yang, K. Wu, et al., Metallic glue for designing composite materials with tailorable properties, *Mater. Horiz.* 8 (6) (2021) 1690–1699.
- [35] J. Schroers, Processing of bulk metallic glass, *Adv. Mater.* 22 (14) (2010) 1566–1597.
- [36] H. Li, Z. Li, J. Yang, et al., Interface design enabled manufacture of giant metallic glasses, *Sci. China Mater.* 64 (4) (2021) 964–972.
- [37] G. Kumar, H.X. Tang, J. Schroers, Nanomoulding with amorphous metals, *Nature* 457 (7231) (2009) 868–872.
- [38] Y. Yan, C. Wang, Z. Huang, et al., Highly efficient and robust catalysts for the hydrogen evolution reaction by surface nano engineering of metallic glass, *J. Mater. Chem. A* 9 (9) (2021) 5415–5424.
- [39] J. Ma, X. Zhang, D. Wang, et al., Superhydrophobic metallic glass surface with superior mechanical stability and corrosion resistance, *Appl. Phys. Lett.* 104 (17) (2014) 173701.
- [40] A. Inoue, A. Takeuchi, Recent development and application products of bulk glassy alloys, *Acta Mater.* 59 (6) (2011) 2243–2267.
- [41] H.J. Tarigan, N. Kahler, N.S. Ramos, et al., Low reflectance of nano-patterned Pt-Cu-Ni-P bulk metallic glass, *Appl. Phys. Lett.* 107 (2) (2015) 021903.
- [42] C. Uzun, C. Meduri, N. Kahler, et al., Photoinduced heat conversion enhancement of metallic glass nanowire arrays, *J. Appl. Phys.* 125 (1) (2019) 015102.
- [43] G. Cai, W. Zhang, L. Jiao, et al., Template-directed growth of well-aligned MOF arrays and derived self-supporting electrodes for water splitting, *Chemistry* 2 (6) (2017) 791–802.
- [44] K. Mizuno, J. Ishii, H. Kishida, et al., A black body absorber from vertically aligned single-walled carbon nanotubes, *Proc. Natl. Acad. Sci. USA* 106 (15) (2009) 6044–6047.
- [45] M. Li, M. Shi, B. Wang, et al., Quasi-ordered nanoforests with hybrid plasmon resonances for broadband absorption and photodetection, *Adv. Funct. Mater.* 31 (38) (2021) 2102840.
- [46] L. Zhou, Y. Tan, D. Ji, et al., Self-assembly of highly efficient, broadband plasmonic absorbers for solar steam generation, *Sci. Adv.* 2 (4) (2016) e1501227.
- [47] D.K. Roper, W. Ahn, M. Hoepfner, Microscale heat transfer transduced by surface plasmon resonant gold nanoparticles, *J. Phys. Chem. C* 111 (9) (2007) 3636–3641.
- [48] H. Ren, M. Tang, B. Guan, et al., Hierarchical graphene foam for efficient omnidirectional solar–thermal energy conversion, *Adv. Mater.* 29 (38) (2017) 1702590.
- [49] Y. Cao, J.-H. Dou, N.-j. Zhao, et al., Highly efficient NIR-II photothermal conversion based on an organic conjugated polymer, *Chem. Mater.* 29 (2) (2017) 718–725.
- [50] B. Lü, Y. Chen, P. Li, et al., Stable radical anions generated from a porous peryleneimide metal-organic framework for boosting near-infrared photothermal conversion, *Nat. Commun.* 10 (1) (2019) 1–8.
- [51] J. Li, X. Liu, L. Tan, et al., Zinc-doped Prussian blue enhances photothermal clearance of *Staphylococcus aureus* and promotes tissue repair in infected wounds, *Nat. Commun.* 10 (1) (2019) 1–15.
- [52] D. Han, Y. Han, J. Li, et al., Enhanced photocatalytic activity and photothermal effects of Cu-doped metal-organic frameworks for rapid treatment of bacteria-infected wounds, *Appl. Catal. B* 261 (2020) 118248.
- [53] D.-L. Han, P.-L. Yu, X.-M. Liu, et al., Polydopamine modified CuS@ HKUST for rapid sterilization through enhanced photothermal property and photocatalytic ability, *Rare Met.* 41 (2) (2022) 663–672.
- [54] Y. Wang, W. Zhu, W. Du, et al., Cocrytals strategy towards materials for near-infrared photothermal conversion and imaging, *Angew. Chem. Int. Ed.* 57 (15) (2018) 3963–3967.
- [55] R. Lv, Y.-Q. Liang, Z.-Y. Li, et al., Flower-like CuS/graphene oxide with photothermal and enhanced photocatalytic effect for rapid bacteria-killing using visible light, *Rare Met.* 41 (2) (2022) 639–649.
- [56] Z.-X. Han, P.-L. Yu, L. Tan, et al., Photothermal-controlled sustainable degradation of protective coating modified Mg alloy using near-infrared light, *Rare Met.* 40 (9) (2021) 2538–2551.
- [57] Y. Luo, B. Li, X. Liu, et al., Simultaneously enhancing the photocatalytic and photothermal effect of NH₂-MIL-125-GO-Pt ternary heterojunction for rapid therapy of bacteria-infected wounds, *Bioact. Mater.* 18 (2022) 421–432.
- [58] C.M. Hessel, V.P. Pattani, M. Rasch, et al., Copper selenide nanocrystals for photothermal therapy, *Nano Lett.* 11 (6) (2011) 2560–2566.
- [59] Y. Yang, Y. Yang, S. Chen, et al., Atomic-level molybdenum oxide nanorings with full-spectrum absorption and photoresponsive properties, *Nat. Commun.* 8 (1) (2017) 1–9.
- [60] H. Li, H. Wen, Z. Zhang, et al., Reverse thinking of the aggregation-induced emission principle: amplifying molecular motions to boost photothermal efficiency of nanofibers, *Angew. Chem. Int. Ed.* 59 (46) (2020) 20371–20375.
- [61] J. Tian, W. Zhang, J. Gu, et al., Bioinspired Au–CuS coupled photothermal materials: enhanced infrared absorption and photothermal conversion from butterfly wings, *Nano Energy* 17 (2015) 52–62.
- [62] B. Guo, Z. Sheng, D. Hu, et al., Through scalp and skull NIR-II photothermal therapy of deep orthotopic brain tumors with precise photoacoustic imaging guidance, *Adv. Mater.* 30 (35) (2018) 1802591.
- [63] X. Ding, C.H. Liow, M. Zhang, et al., Surface plasmon resonance enhanced light absorption and photothermal therapy in the second near-infrared window, *J. Am. Chem. Soc.* 136 (44) (2014) 15684–15693.
- [64] Z.C. Wu, W.P. Li, C.H. Luo, et al., Rattle-type Fe₃O₄@ CuS developed to conduct magnetically guided photoinduced hyperthermia at first and second near-infrared biological windows, *Adv. Funct. Mater.* 25 (41) (2015) 6527–6537.



Jianan Fu received the B.S. degree from Jiangxi Agricultural University in 2019 and the master degree in mechanical engineering from Shenzhen University in 2022. He will study for a PhD at Southern University of science and technology. His research includes micro/nano-structure by the thermoplastic forming process and functional application of metallic glasses.



Jiang Ma received the B.S. degree in materials science and engineering from Southeast University in 2009 and the Ph.D. degree from the Institute of Physics, Chinese Academy of Sciences (CAS), Beijing, China, in 2014, and received the Outstanding PhD student Award (Top 1%) and Institute Director Honored Award (Top 5%). He is currently a Professor in the College of Mechatronics and Control Engineering, Shenzhen University, China, and received the Outstanding Teacher Award of Shenzhen, 2018. His research includes the forming, functional application and high frequency dynamic loading behavior of metallic glasses.